






Atomic structural mechanism for ferroelectric-antiferroelectric transformation in perovskite NaNbO_3

Cho Sandar Htet ¹, S. Nayak,^{1,2} Alicia Manjón-Sanz ³, J. Liu,³ J. Kong,¹ D. R. Sørensen ^{4,6}, F. Marlton,⁵ M. R. V. Jørgensen ^{4,6} and A. Pramanick ^{1,7,*}

¹Department of Materials Science and Engineering, City University of Hong Kong, Hong Kong, China

²Department of Physics, Indian Institute of Technology Madras, Chennai-600036, India

³Neutrons Scattering Division, Oak Ridge National Laboratory, Oak Ridge, Tennessee 37831, USA

⁴Department of Chemistry and iNANO, Aarhus University, 8000 Aarhus C, Denmark

⁵Department of Chemistry, University of Sydney, NSW 2006, Australia

⁶MAX IV Laboratory, Lund University, SE-221 00, Lund, Sweden

⁷Center for Neutron Scattering, City University of Hong Kong, Hong Kong, China



(Received 14 February 2022; revised 29 April 2022; accepted 9 May 2022; published 31 May 2022)

Sodium niobate (NaNbO_3 or NN) is described as “the most complex perovskite system,” which exhibits transitions between, as well as coexistence of, several ferroelectrics (FE) and antiferroelectric (AFE) phases at different temperatures. Recently, solid solutions of NN with stabilized AFE phases(s) have gained attention for energy-related applications, such as high-density energy storage and electrocaloric cooling. A better understanding of the atomic mechanisms responsible for AFE/FE phase transitions in NaNbO_3 can enable a more rational design of its solid-solution systems with tunable functional properties. Here, we have investigated changes in the average and local atomic structure of NN using a combination of x-ray/neutron diffraction and neutron pair-distribution function (PDF) analyses. The Rietveld refinement of the x-ray/neutron-diffraction patterns indicates a coexistence of the FE Q ($P2_1ma$) and AFE P ($Pbma$) phases in the temperature range of $300\text{ K} \leq T \leq 615\text{ K}$, while PDF analysis indicated that the local structure ($r < 8\text{ \AA}$) is better described by a $P2_1ma$ symmetry. Above 615 K, the average structure transitions to an AFE R phase ($Pmnm$ or $Pnma$), while PDF analysis shows an increased disordering of the octahedral distortions and Na displacements at the local scale. These results indicate that the average $P/Q/R$ phase transitions in NN can be described as a result of complex ordering of distorted octahedral tilts at the nanoscale and off-centered displacements of the Na atoms.

DOI: [10.1103/PhysRevB.105.174113](https://doi.org/10.1103/PhysRevB.105.174113)

I. INTRODUCTION

Polymorphic phase transitions are commonly observed in ABO_3 perovskite compounds as a result of various structural distortions, such as stretching of AO bonds and distortions or tilting of BO_6 octahedra [1,2]. Among the known perovskites, NaNbO_3 exhibits the most complex series of polymorphic phase transitions as a function of temperature. The early crystallographic works on NaNbO_3 were undertaken by Megaw and co-workers [3–9]. In their 1974 paper, Megaw *et al.* summarized the seven phases of NaNbO_3 as paraelectric U phase with cubic $Pm\bar{3}m$ structure ($> 640\text{ }^\circ\text{C}$), paraelectric $T2$ phase with tetragonal $F4/mmm$ structure ($575\text{--}640\text{ }^\circ\text{C}$), paraelectric $T1$ phase with orthorhombic $Cmcm$ structure ($520\text{--}575\text{ }^\circ\text{C}$), paraelectric S phase with orthorhombic $Pnmm$ structure ($480\text{--}520\text{ }^\circ\text{C}$), antiferroelectric (AFE) R phase with orthorhombic $Pnmm$ structure ($360\text{--}480\text{ }^\circ\text{C}$), AFE P phase with orthorhombic $Pbma$ structure ($-100\text{--}360\text{ }^\circ\text{C}$), and ferroelectric (FE) N phase with rhombohedral $R3c$ structure (below $-100\text{ }^\circ\text{C}$) [9]. In addition, an FE Q phase with orthorhombic

$P2_1ma$ structure was listed, which coexists with the P phase at room temperature and furthermore can be induced from the P phase under applied electric fields [3]. Later x-ray/neutron-diffraction and Raman-scattering studies confirmed the above sequence of structural phase transitions, while also showing additional possible polymorphs of NaNbO_3 , depending on particle morphology and external conditions [10–18]. For example, in 70-nm fine NaNbO_3 powders, an orthorhombic $Pmma$ structure was reported by Shiratori *et al.* [19]. The same authors also reported irreversible phase transitions in submicron- and nanocrystalline NaNbO_3 under pressure of 2–10 GPa, which are likely caused by reorientation of NbO_6 octahedra [20]. Additionally, it was reported that NaNbO_3 also exhibits another phase with incommensurate modulation of octahedral rotations, which is reflected from a diffuse dielectric peak at $\sim 170\text{ }^\circ\text{C}$ [12,21]. The rich phase diagram of NaNbO_3 containing nonpolar, antiferroelectric, and ferroelectric phases has confounded researchers over the years, despite its seemingly simple chemistry, such that NaNbO_3 has been described as “the most complex perovskite system known” [1].

From an applications point of view, NaNbO_3 is of tremendous interest because of its various attractive

*apramani@cityu.edu.hk

functional properties. NaNbO_3 is characterized as an AFE. Due to their characteristic double polarization-electric field (P - E) hysteresis loops with high maximum polarization ($P_{\text{max}} \sim 40 \mu\text{C}/\text{cm}^2$) and small remanent polarization ($P_{\text{rem}} < 5 \mu\text{C}/\text{cm}^2$), AFEs are attractive for high-density, high-power energy-storage applications [22]. Ultrahigh-energy-storage density has been recently reported in bulk ceramics and thin films of solid solutions of NaNbO_3 [23–25]. In addition, NaNbO_3 also exhibits attractive optical, electrocaloric, and energy-harvesting properties [26–28]. NaNbO_3 is also the end member of the $(\text{K},\text{Na})\text{NbO}_3$ solid-solution system, which has shown potential as an attractive Pb-free piezoelectric material [29]. Such a broad array of attractive functionalities has led to a renewed interest for more thorough understanding of the structure of NaNbO_3 . It is expected that a better atomistic understanding of the structural transitions in NaNbO_3 could help to stabilize the different phases, which are desirable from an application point of view, such as the P phase for energy storage [30] or R phase for electrocaloric applications [24,31,32].

In recent years, several theoretical and experimental studies have been undertaken to explain the microscopic origins of the broad array of phase transitions in NaNbO_3 . Theoretical calculations by Mishra *et al.* revealed that the free-energy difference between the AFE and FE phases is comparable to the scale of thermal fluctuations, which can explain their coexistence and easy transformation under temperature changes or external variables such as an electric field [18]. Another interesting hypothesis is that the appearance of long-range AFE and FE phases is caused by an irregular arrangement of nanoscale twins, which results from complex local octahedral tilting patterns, possibly coupled to off-centered Na displacements with high-energy barriers [33,34]. A corollary of this latter view is that since the different structures could be ultimately related to the subtly different arrangements of nanoscale twins, determination of local atomic structure can help to understand the structural complexities of NaNbO_3 . The local environment of Nb in the different possible polymorphs of NaNbO_3 was examined by Johnston *et al.* using solid-state NMR, which indicated similar local structures for AFE $Pbcm$ and FE $P2_1ma$ polymorphs [33,35]. Consequently, Johnston *et al.* described the $Pbcm$ structure to result from a twinning operation of the $P2_1ma$ structure; however, that study did not reveal the details for such twinning operation [33]. Similar conclusions were reached by Jiang *et al.* from neutron pair-distribution function (PDF) experiments, although that study indicated the local structure to be $R3c$ and not $Pbcm$ or $P2_1ma$ [34]. Although these earlier studies indicated possible atomistic mechanisms for the different phase transitions in NaNbO_3 , they did not provide a comprehensive picture of temperature-dependent evolution of octahedral distortion and tilting in the local and average structures. Here, we reexamined the temperature-dependent changes in the average and local structures of NaNbO_3 to reveal the structural relationship between the P and Q phases, and furthermore the local atomic mechanism for transformation from the AFE P phase to the AFE R phase. Our results indicate that the relative volume fractions of P and Q phases below 615 K can be described as a result of twinning of local $P2_1ma$ structural

blocks, while transformation from P/Q phase to R phase results from further disordering of Na displacements.

II. EXPERIMENT

Powder samples of NaNbO_3 were prepared by the conventional solid-state reaction method. The precursor compounds of Na_2CO_3 (Sigma-Aldrich, 99.9%) and Nb_2O_5 (Sigma-Aldrich, 99.9%) in powder form were dried at 100 °C in an oven for 24 h to remove any moisture. The dried powder samples were subsequently combined according to stoichiometric ratio, and ball milled for 24 h using ethanol as solvent and zirconia balls as the milling media. The mixed slurry was dried overnight at 100 °C and subsequently calcined at 1100 °C for 3 h in oxygen atmosphere. The calcined product was ball milled for another 24 h, dried and then ground together with 5% polyvinyl alcohol (PVA) as a binder, and finally sieved through a 100- μm mesh. Green pellets of 10-mm diameter were prepared by pressing the mix of calcined powder and PVA under a uniaxial pressure of 30 MPa. After that the pellets were placed in alumina crucible and sintered at 1350 °C for 2 h in air atmosphere to obtain the desired products. The NaNbO_3 pellets were ground using an agate mortar and pestle and sieved through a 100- μm mesh for neutron and x-ray diffractions and differential scanning calorimetry (DSC) experiments. During sintering, the pellets were covered with powders of the same composition to mitigate volatilization of metal atoms.

The DSC measurement was performed using a Netzsch DSC setup (model- STA 449F3) at a heating rate of 10 K/min. Powder x-ray diffraction measurement at 300 K was performed at the DanMAX beamline of the MAX IV Laboratory. The samples were packed in 0.3-mm glass capillaries. Data were collected for up to a maximum momentum transfer of $Q \sim 10.8 \text{ \AA}^{-1}$ using x rays of wavelength 0.3529 Å and a DECTRIS PILATUS3 X 2M CdTe detector. The raw area detector data were azimuthally integrated using the PYFAI library [36]. Time-of-flight neutron-scattering measurements were conducted at the Spallation Neutron Source (Oak Ridge National Laboratory). Neutron-diffraction (ND) experiments were performed at the POWGEN instrument [37]. Approximately 2 g of NaNbO_3 powder sample was sealed in a 6-mm-diameter vanadium can with helium exchange gas and loaded in the POWGEN automatic changer. The data were collected in the temperature range $300 \text{ K} \leq T \leq 673 \text{ K}$ while heating using a heating rate of 5 K/min. The measurement time at each temperature was approximately 2.5 h. A central wavelength of 0.8 Å was used covering a d spacing of 0.16–6.77 Å. Total neutron-scattering-measurements were conducted at the NOMAD instrument equipped with an ILL furnace [38]. The sample was loaded into a vanadium can of 3-mm diameter and 20-mm length. Measurements were done in the temperature range of $300 \text{ K} \leq T \leq 673 \text{ K}$. Four 24-min scans were collected and then summed together to improve the statistics. In order to subtract the background intensity, the scattering pattern of an empty vanadium can was taken. The background-corrected intensity was subsequently normalized against proton charge and scattering from a 6-mm vanadium rod to correct for neutron flux and detector efficiency,

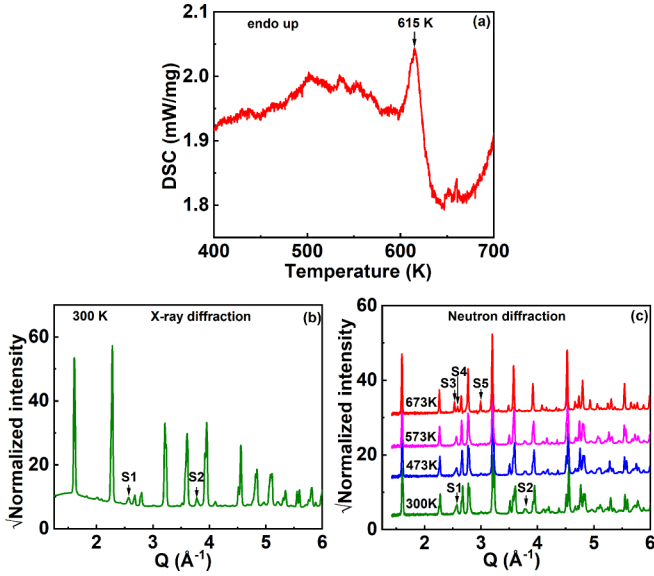


FIG. 1. Temperature-dependent structural changes in NaNbO_3 : (a) DSC profile for NaNbO_3 powder measured in the temperature range of $300 \text{ K} \leq T \leq 700 \text{ K}$, showing the endothermic peak (pointing up) at $T \sim 615 \text{ K}$. Also note a broad anomaly in the DSC curve in the temperature range between 450 and 600 K. (b) X-ray diffraction pattern of NaNbO_3 powder measured at 300 K. (c) Neutron-diffraction patterns measured in the temperature range of $300 \text{ K} \leq T \leq 673 \text{ K}$. The characteristic superlattice reflections for the antiferroelectric phases are marked with arrows.

respectively. The reduced pair-distribution function, $G(r)$, was obtained using the equation

$$G(r) = \left(\frac{2}{\pi}\right) \int_{Q_{\min}}^{Q_{\max}} Q(S(Q) - 1) \sin(Qr) dQ, \quad (1)$$

where $G(r)$ is related to the atom-pair density function $\rho(r)$ and the pair distribution function $g(r)$ through the following relations:

$$G(r) = 4\pi r[\rho(r) - \rho_0] = 4\pi r\rho_0[g(r) - 1], \quad (2)$$

where ρ_0 is the atomic number density [39,40]. We used a Q_{\min} of 0.5 \AA^{-1} and Q_{\max} of 25 \AA^{-1} . It is worth noting that the distinct scattering function was not absolutely normalized according to the sample number density. Instead, it is scaled according to the ratio of the normalized scattering power between vanadium rod and sample at Q_{\max} of 25 \AA^{-1} [38]. Also, the small-angle scattering intensity below Q_{\min} was excluded from the Fourier transformation process.

III. RESULTS AND DISCUSSION

A. Average structure analysis of NaNbO_3

Figure 1(a) shows the heat-flow curve of NaNbO_3 as a function of temperature upon heating, which was measured using DSC in the range of $400 \text{ K} \leq T \leq 700 \text{ K}$. A clear anomaly can be observed at $T \sim 615 \text{ K}$, which is coincident with the $P \rightarrow R$ phase transition that was identified in earlier studies [9]. In addition, we observe a broad anomaly over the temperature range of 440–580 K, which is similar to the temperature range where a broad anomaly in the dielectric

permittivity spectrum was also observed, possibly as a result of incommensurate structural modulations of the P -phase structure [21].

To understand the details of the structural phase transitions in NaNbO_3 (NN), we performed powder x-ray and neutron-diffraction experiments. Figure 1(b) shows the powder-diffraction pattern measured using synchrotron x rays at 300 K. Figure 1(c) shows the temperature-dependent powder-diffraction patterns measured using neutrons as a function of temperature during heating from 300 to 673 K. In addition to the hkl Bragg reflections for a pseudocubic perovskite unit cell, we also observed the appearance of superlattice (SL) peaks at different temperatures, which are marked with arrows and labeled as S1, S2, S3, S4, and S5 in Figs. 1(b) and 1(c). At 300 K, the SL peaks S1 and S2 are visible in the x-ray diffraction pattern at $Q \sim 2.51 \text{ \AA}^{-1}$ and $Q \sim 3.77 \text{ \AA}^{-1}$; the same SL peaks are also observed in the neutron-diffraction patterns measured in the temperature range of 300–573 K. These SL peaks arise due to the tilting of oxygen octahedra [18]. At 673 K, the SL peaks of S1 and S2 disappear, while additional SL peaks appear in the neutron-diffraction pattern at $Q \sim 2.6, 2.75, \text{ and } 3 \text{ \AA}^{-1}$, which are labeled as S3, S4, and S5. The clear changes in the SL peaks above 573 K indicate a phase transition [41,42], which is consistent with the anomaly observed in the DSC data in Fig. 1(a) at $T \sim 615 \text{ K}$.

The temperature-dependent changes in the average crystal structure of NaNbO_3 were characterized from Rietveld refinement using x-ray and neutron Bragg diffraction data using the software GSAS II [43]. We undertook a combined Rietveld refinement using both the neutron (POWGEN) and x-ray (DanMAX) diffraction data measured at 300 K. For all other temperatures, Rietveld refinement was performed using only neutron diffraction data. Different structural models were tried for fitting of the Bragg peaks, *viz.*, $Pbma$, $P2_1ma$, $Pmnn$, and $Pnma$ using the models provided in Refs. [18,33–35,41,42,44] Lattice parameters, atomic coordinates, and isotropic atomic displacement parameters (ADPs), together with background coefficient and sample related peak-profile parameters, were refined to best fit the experimental Bragg diffraction data. The quality of the fits was determined from the weighted residuals R_w [45].

For fitting of the diffraction data below $T = 615 \text{ K}$, Rietveld refinement was first performed using either $Pbma$ (P -phase) (Figs. S1(a)–S1(d) in the Supplemental Material [46]) or $P2_1ma$ (Q -phase) (Figs. S2(a)–S2(d) in the Supplemental Material [46]) space groups, separately. In both cases, the obtained R_w were less than 10% for all temperatures, although the $Pbma$ structure model had a slightly lower R_w as compared to that of the $P2_1ma$ structure model. However, while there was general agreement between the observed and the fitted patterns with regard to the main Bragg peaks, use of either the P or Q phase alone could not satisfactorily reproduce the SL peaks present at $Q \sim 2.53 \text{ \AA}^{-1}$ and 2.99 \AA^{-1} ; see insets in Figs. S1(a)–S1(d) and S2(a)–S2(d). Therefore, we next tried fitting of the Bragg diffraction peaks using a two-phase mixture of $Pbma$ and $P2_1ma$ structures, the results of which are shown in Figs. 2 and 3. Rietveld refinement using a two-phase mixture of $Pbma$ and $P2_1ma$ structures could fit the diffraction data better at all temperatures below

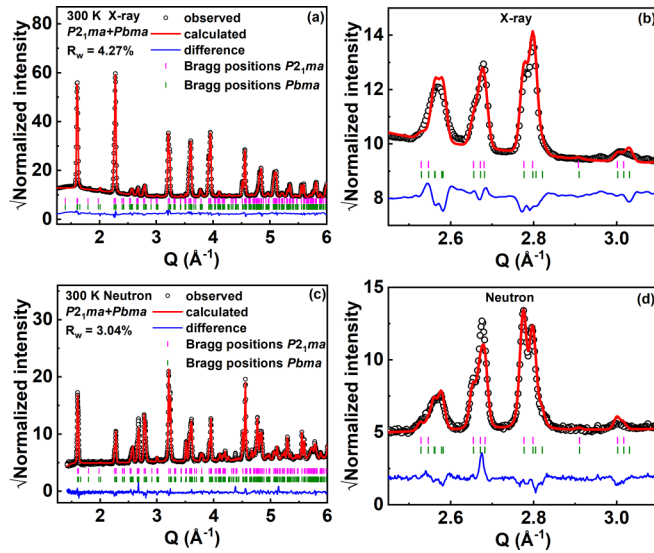


FIG. 2. Rietveld refinement of NaNbO_3 using combined x-ray and neutron-diffraction data measured at 300 K: (a), (b) x-ray diffraction data; (c), (d) neutron-diffraction data. A two-phase mixture consisting of structures with $Pbma$ (P phase) and $P2_1ma$ (Q phase) space groups is used to fit the measured diffraction patterns. The superlattice reflections present in the region of $Q = 2.45\text{--}3.1\text{ \AA}^{-1}$ are shown in the enlarged views of the (b) x-ray and (d) neutron-diffraction patterns. Observed (black symbols), calculated (red line), difference (blue line) profiles, and Bragg positions (green and pink ticks) obtained after the Rietveld refinement using GSAS II software. Weighted residuals (R_w) are shown for all the refinements.

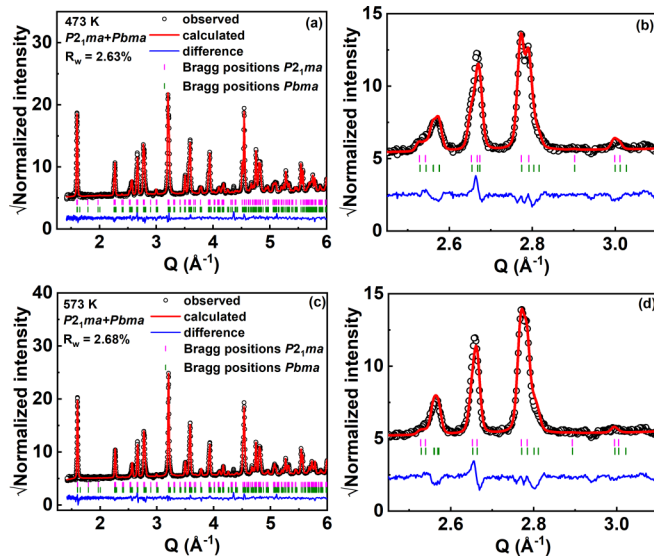


FIG. 3. Rietveld refinement of NaNbO_3 using neutron-diffraction data measured. (a), (b) 473 K and (c), (d) 573 K. A two-phase mixture consisting of structures with $Pbma$ (P phase) and $P2_1ma$ (Q phase) is used to fit the measured diffraction patterns. The superlattice reflections present in the region of $Q = 2.45\text{--}3.1\text{ \AA}^{-1}$ is shown in (b). Observed (black symbols), calculated (red line), difference (blue line) profiles, and Bragg positions (green and pink ticks) obtained after the Rietveld refinement using GSAS II software. Weighted residuals (R_w) are shown for all the refinements.

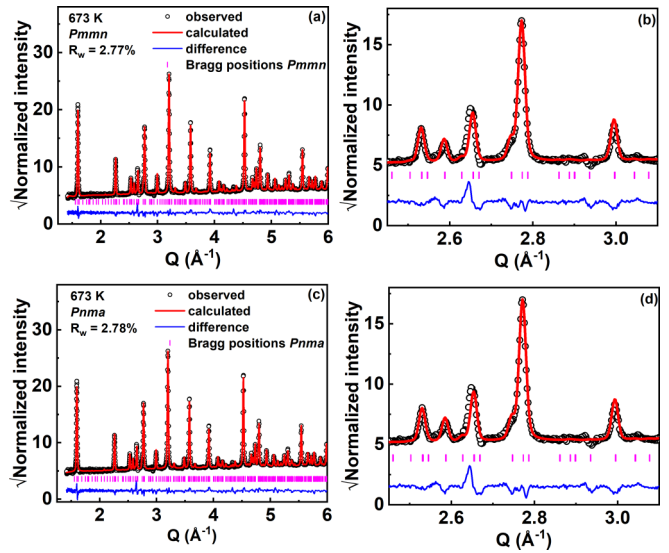


FIG. 4. Rietveld refinement of NaNbO_3 using neutron-diffraction data measured at 673 K using (a), (b) $Pmnm$ and (c), (d) $Pnma$ space groups for R -phase structure. The superlattice reflections present in the region of $Q = 2.45\text{--}3.1\text{ \AA}^{-1}$ are shown in (b) and (d). Observed (black symbols), calculated (red line), difference (blue line) profiles, and Bragg positions (green and pink ticks) obtained after the Rietveld refinement using GSAS II software. Weighted residuals (R_w) are shown for all the refinements.

615 K, as compared to using either of the $Pbma$ or $P2_1ma$ structures alone. More importantly, using a two-phase mixture for Rietveld refinement improved fitting of the SL peaks in the range of $Q \sim 2.45$ to 3.10 \AA^{-1} , which are shown in Figs. 2(b) and 2(d) and 3(b) and 3(d).

The neutron-diffraction patterns measured at 673 K are shown in Fig. 4. There is a clear change in the SL peaks observed in the range of $Q \sim 2.45$ to 3.10 \AA^{-1} , as shown in Figs. 4(b) and 4(d), which indicates a structural transformation. This is also consistent with the peak observed in the DSC curve at $T \sim 615\text{ K}$, as shown in Fig. 1(a). As shown in Figs. S1(e) and S2(e), use of either of the $Pbma$ or $P2_1ma$ structures did not yield a good fit for the SL peaks observed at 673 K [46]. In earlier works, the structure above 633 K was described as an R phase. In order to fit the Bragg diffraction data at 673K, we tried the space groups $Pnma$ and $Pmnm$, which could describe the average R phase structure, such as reported in Refs [42,43]. The refinements using the $Pmnm$ and $Pnma$ space groups separately yielded $R_w \sim 2.77\%$ and $R_w \sim 2.78\%$, respectively. This indicates that either the $Pmnm$ or $Pnma$ structure model could be used to describe the average structure equally well. However, the ADPs are slightly lower for the $Pmnm$ structure (see Table I), which may indicate that it is the more suitable model. We have further examined the appropriateness of the $Pmnm$ or $Pnma$ structural models in the next section.

The detailed structural parameters obtained from the Rietveld refinement using diffraction data at different temperatures are listed in Table I. The unit-cell parameters as a function of temperature for all the phases are shown in Figs. 5(a)–5(c). For easy comparison, the lattice parameters of the $P/Q/R$ phases were converted to their equivalent pseu-

TABLE I. Structural parameters, fractional atomic coordinates, and equivalent isotropic displacement parameters (U_{iso} in \AA^2) from combined Rietveld refinement results of x-ray and neutron data at 300 K and Rietveld refinement results of neutron data from 473 to 673 K of NaNbO_3 .

TEMPERATURE: 300 K									
Phase 1(<i>Pbma</i>)					Phase 2(<i>P2₁ma</i>)				
Atoms	<i>X</i>	<i>Y</i>	<i>Z</i>	U_{iso}	Atoms	<i>X</i>	<i>Y</i>	<i>Z</i>	U_{iso}
Na ₁	0.75 000	0.00000	0.2540(21)	0.0123(13)	Na ₁	0.278(4)	0.000 00	0.770(4)	0.023(3)
Na ₂	0.777 3(15)	0.250 00	0.2539(20)	0.0115(11)	Na ₂	0.290(4)	0.500 00	0.733(3)	0.0175(27)
Nb ₁	0.273 9(4)	0.124 94(17)	0.2474(5)	0.0026(22)	Nb ₁	0.2606(6)	0.2514(7)	0.2447(8)	0.0068(6)
O ₁	0.2500 0	0.000 00	0.3039(11)	0.0042(9)	O ₁	0.2477(15)	0.000 00	0.2847(19)	0.0068(15)
O ₂	0.226 2(7)	0.250 00	0.1779(8)	0.0043(6)	O ₂	0.2285(10)	0.5000 0	0.1942(15)	0.0010(11)
O ₃	0.032 9(5)	0.141 02(17)	0.5393(5)	0.0082(4)	O ₃	0.0025(10)	0.27 89(9)	0.5063(12)	0.0179(13)
O ₄	0.457 7(5)	0.109 64(17)	-0.0377(5)	0.0054(4)	O ₄	0.0524(8)	0.2202(7)	0.0431(10)	0.0047(7)
Lattice parameters (\AA)					Lattice parameters (\AA)				
$a = 5.5689 1(7) b = 15.528 29(27) c = 5.505 12(8)$					$a = 5.569 93(11) b = 7.763 56(29) c = .505 02(16)$				
$\alpha = \beta = \gamma = 90^\circ$					$\alpha = \beta = \gamma = 90^\circ$				
Cell volume = 476.059(10) \AA^3					Cell volume = 238.051(10) \AA^3				
					Phase ratio				
					Phase 1 = 49.31%, Phase 2 = 50.69%				
TEMPERATURE:473K									
Phase 1(<i>Pbma</i>)					Phase 2(<i>P2₁ma</i>)				
Atoms	<i>X</i>	<i>Y</i>	<i>Z</i>	U_{iso}	Atoms	<i>X</i>	<i>Y</i>	<i>Z</i>	U_{iso}
Na ₁	0.750 00	0.000 00	0.242(4)	0.0192(23)	Na ₁	0.293(6)	0.000 00	0.762(7)	0.029(6)
Na ₂	0.767 2(20)	0.250 00	0.250(4)	0.0163(20)	Na ₂	0.284(9)	0.500 00	0.734(9)	0.046(8)
Nb ₁	0.268 1(4)	0.124 9(3)	0.2486(8)	0.0052(3)	Nb ₁	0.2680(10)	0.252 7(12)	0.2504(15)	0.0095(11)
O ₁	0.250 00	0.000 00	0.2914(10)	0.0069(10)	O ₁	0.2526(24)	0.000 00	0.3340(25)	0.0114(22)
O ₂	0.228 4(12)	0.250 00	0.1902(12)	0.0085(11)	O ₂	0.2253(15)	0.500 00	0.1808(18)	0.0004(10)
O ₃	0.030 8(9)	0.138 91(28)	0.5346(8)	0.0122(7)	O ₃	0.0073(16)	0.2828(15)	0.5085(20)	0.0189(19)
O ₄	0.461 6(8)	0.111 59(26)	-0.0345(8)	0.0100(5)	O ₄	-0.0502(12)	0.2176(13)	0.0401(17)	0.0101(13)
Lattice parameters (\AA)					Lattice parameters (\AA)				
$a = 5.56742(17) b = 15.5925(7) c = 5.51448(18)$					$a = 5.5695(4) b = 7.7953(8) c = 5.5157(4)$				
$\alpha = \beta = \gamma = 90^\circ$					$\alpha = \beta = \gamma = 90^\circ$				
Cell volume = 478.711(25) \AA^3					Cell volume = 239.473(29) \AA^3				
					Phase ratio				
					Phase 1 = 53.14%, Phase 2 = 46.86%				
TEMPERATURE: 573 K									
Phase 1(<i>Pbma</i>)					Phase 2(<i>P2₁ma</i>)				
Atoms	<i>X</i>	<i>Y</i>	<i>Z</i>	U_{iso}	Atoms	<i>X</i>	<i>Y</i>	<i>Z</i>	U_{iso}
Na ₁	0.750 00	0.000 00	0.257(4)	0.023(20)	Na ₁	0.395(18)	0.000 00	0.886(19)	0.038(18)
Na ₂	0.766 6(23)	0.250 00	0.254(3)	0.025 4(20)	Na ₂	0.339(24)	0.50 000	0.691(25)	0.07(4)
Nb ₁	0.259 9(5)	0.124 9(5)	0.2496(8)	0.009 23(27)	Nb ₁	0.2657(23)	0.252 6(19)	0.2492(21)	0.0024(11)
O ₁	0.250 00	0.000 00	0.3187(10)	0.012 9(12)	O ₁	0.258(5)	0.000 00	0.269(4)	0.001(20)
O ₂	0.232 0(10)	0.250 00	0.2064(10)	0.009 4(11)	O ₂	0.214(4)	0.50 000	0.209(4)	0.0004(4)
O ₃	0.026 8(9)	0.139 44(28)	0.5298(8)	0.016 1(8)	O ₃	0.011(4)	0.260(4)	0.498(5)	0.0105(24)
O ₄	0.463 4(8)	0.111 47(27)	-0.0319(8)	0.013 8(6)	O ₄	-0.0513(24)	0.233 6(20)	0.0492(29)	0.0025(17)
Lattice parameters (\AA)					Lattice parameters (\AA)				
$a = 5.564 14(8) b = 15.64974(24) c = 5.523 42(8)$					$a = 5.5659(4) b = 7.8264(6) c = 5.5246(4)$				
$\alpha = \beta = \gamma = 0^\circ$					$\alpha = \beta = \gamma = 90^\circ$				
Cell volume = 480.965(13) \AA^3					Cell volume = 240.658(22) \AA^3				
					Phase ratio				
					Phase 1 = 83.59%, Phase 2 = 16.41%				

TABLE I. (*Continued.*)

TEMPERATURE: 673 K					
Phase (<i>Pnma</i>)					
Atoms	X	Y	Z	Uiso	
Na ₁	0.011(11)	0.250 00	0.003(4)	0.032(17)	
Na ₂	0.008(8)	0.250 00	0.837(4)	0.030(13)	
Na ₃	0.022(7)	0.250 00	0.664(5)	0.033(13)	
Na ₄	−0.010(10)	0.250 00	0.503(4)	0.029(14)	
Na ₅	−0.024(6)	0.250 00	0.337(3)	0.023(10)	
Na ₆	−0.005(8)	0.250 00	0.163(5)	0.030(14)	
Nb ₁	0.7523(27)	0.003 4(30)	0.9140(9)	0.0084(18)	
Nb ₂	0.7512(27)	0.003 2(31)	0.0836(10)	0.0087(17)	
Nb ₃	0.7490(19)	−0.001 2(30)	0.2526(10)	0.0082(11)	
O ₁	0.769(4)	0.250 00	0.4033(14)	0.015(5)	
O ₂	0.714(5)	0.250 00	0.5929(13)	0.017(5)	
O ₃	0.776(4)	0.250 00	0.7414(12)	0.014(5)	
O ₄	0.782(5)	0.250 00	0.9265(16)	0.016(6)	
O ₅	0.717(4)	0.250 00	0.0756(13)	0.012(4)	
O ₆	0.744(3)	0.250 00	0.2582(12)	0.009(3)	
O ₇	0.722(4)	−0.022(3)	−0.0003(17)	0.020(4)	
O ₈	0.7786(25)	0.024 8(24)	0.1670(26)	0.0170(30)	
O ₉	0.7167(25)	−0.030 8(25)	0.3329(18)	0.0199(27)	
O ₁₀	0.0014(21)	−0.026 9(31)	0.9263(9)	0.015(3)	
O ₁₁	−0.0017(19)	−0.002 5(25)	0.2590(8)	0.0107(23)	
O ₁₂	−0.0018(31)	−0.027 4(30)	0.4069(10)	0.014(4)	

Lattice parameters (Å)

$$a = 7.851\,92(18) \quad b = 7.848\,60(20) \quad c = 23.5389(6)$$

$$\alpha = \beta = \gamma = 90^\circ$$

$$\text{Cell volume} = 1450.625(29) \text{ \AA}^3$$

TEMPERATURE: 673 K					
Phase (<i>Pmnm</i>)					
Atoms	X	Y	Z	Uiso	
Na ₁	0.250 00	0.082(4)	0.263(13)	0.030(20)	
Na ₂	0.250 00	0.079(4)	0.770(9)	0.028(15)	
Na ₃	0.250 00	0.250 00	0.225(12)	0.018(12)	
Na ₄	0.250 00	0.250 00	0.766(15)	0.026(22)	
Na ₅	0.250 00	0.581(4)	0.262(16)	0.031(19)	
Na ₆	0.250 00	0.578(4)	0.740(11)	0.031(19)	
Na ₇	0.250 00	0.750 00	0.236(16)	0.030(25)	
Na ₈	0.250 00	0.750 00	0.718(11)	0.023(14)	
Nb ₁	0.000 00	0.000 00	0.000 00	0.009(4)	
Nb ₂	0.000 00	0.0000 0	0.500 00	0.009(4)	
Nb ₃	0.000 4(18)	0.169 2(6)	−0.002 1(24)	0.0086(30)	
Nb ₄	0.001 3(18)	0.165 3(5)	0.499 6(23)	0.0087(30)	
O ₁	0.035 4(24)	−0.009 4(11)	0.247 7(26)	0.014(3)	
O ₂	−0.014 4(28)	0.176 1(11)	0.250 9(28)	0.0135(30)	
O ₃	0.011 1(27)	0.157 2(10)	0.756 5(22)	0.0135(31)	
O ₄	−0.026(7)	0.081 9(10)	0.029(4)	0.019(8)	
O ₅	0.028(7)	0.0814(10)	0.473(4)	0.018(8)	
O ₆	0.031(8)	0.25000	−0.028(5)	0.019(9)	
O ₇	−0.020(8)	0.25000	0.535(5)	0.020(10)	
O ₈	0.250 00	0.0102(19)	−0.035(4)	0.017(6)	
O ₉	0.250 00	−0.0099(16)	0.540(4)	0.012(5)	
O ₁₀	0.250 00	0.1594(18)	0.020(4)	0.014(6)	
O ₁₁	0.250 00	0.1738(18)	0.493(5)	0.017(6)	
O ₁₂	0.250 00	0.6775(16)	0.005(4)	0.015(7)	
O ₁₃	0.250 00	0.6569(15)	0.477(5)	0.014(6)	

Lattice parameters (Å)

$$a = 7.8440(6) \quad b = 23.5263(17) \quad c = 7.8469(6)$$

$$\alpha = \beta = \gamma = 90^\circ$$

$$\text{Cell volume} = 1448.08(23) \text{ \AA}^3$$

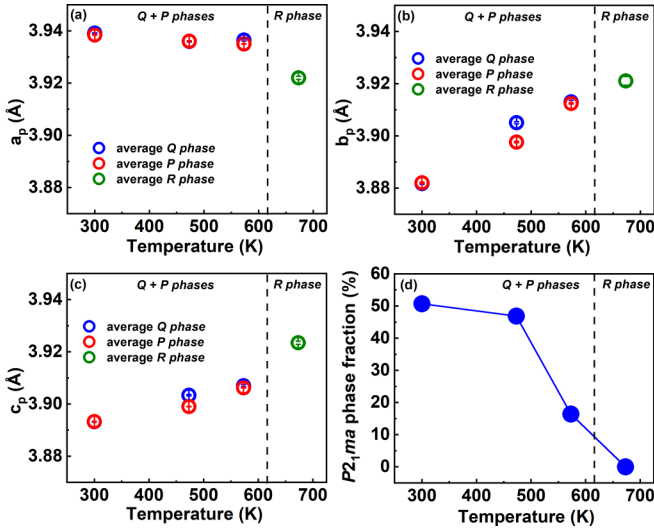


FIG. 5. (a), (b), (c) Changes in the equivalent lattice parameters (a) a_p , (b) b_p , and (c) c_p , as a function of temperature from 300 to 673 K, where a_p , b_p , and c_p correspond to pseudocubic unit cell of elementary perovskite structure (refer to text). For the sake of easy comparison with the corresponding cell parameters of the various phases of NaNbO₃, we have plotted equivalent elementary lattice parameters instead of lattice parameters corresponding to the different phases. (d) The phase fraction of $P2_1ma$ space group was obtained from average Rietveld refinement as a function of temperature in the range of $300 \text{ K} \leq T \leq 673 \text{ K}$.

docubic unit-cell parameters using the relations $a_p = a/\sqrt{2}$, $b_p = b/2$, $c_p = c\sqrt{2}$ for $P2_1ma$, $a_p = a/\sqrt{2}$, $b_p = b/4$, $c_p = c\sqrt{2}$ for $Pbma$ and $a_p = a/2$, $b_p = b/6$, $c_p = c/2$ for $Pmmn$, where the subscript p denotes unit cell of the pseudocubic perovskite structure. With increasing temperature over the range of $300 \text{ K} \leq T \leq 600 \text{ K}$, the “small” [Fig. 5(b)] and “medium” [Fig. 5(c)] unit-cell dimensions monotonically increase, while the “large” [Fig. 5(a)] unit-cell dimension remains relatively unchanged. These trends are consistent with the results from Mishra *et al.* [42]. Above 615 K, there is a discontinuous change in the lattice parameters, whereby the values of small, medium, and large unit-cell dimensions approach each other, which is also similar to the observation of Peel *et al.* [41].

Figure 5(d) shows changes in the relative volume phase fractions of the Q ($P2_1ma$) phase as a function of temperature. At 300 K, there is a nearly equal coexistence of the P (50.7%) and Q (49.3%) phases. This result is different than the earlier report by Mishra *et al.*, which concluded that the P phase is present predominantly ($\sim 99\%$) at 300 K [18]. This could be due to the better resolution of the Bragg peaks in the current measurement, especially a clearer splitting of the SL peaks; additionally, both neutron and x-ray Bragg data are used for the current refinements, while the earlier analysis used only neutron data [18]. Our results, however, agree with Johnston *et al.*, who reported that the phase fraction of the Q phase could be as high as 40–50% [33]. The difference in phase fraction of the Q phase may originate due to different synthesis conditions [33].

Interestingly, the pseudocubic lattice parameters for both the P and Q phases are very similar, and they exhibit similar

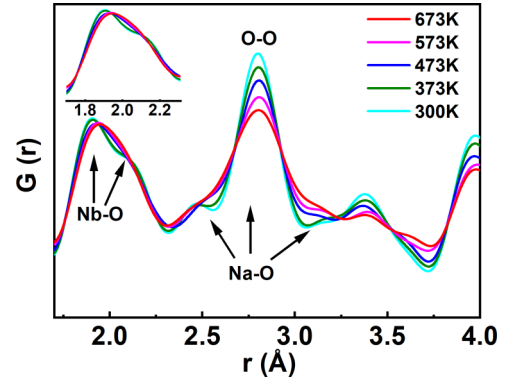


FIG. 6. Neutron pair-distribution function $G(r)$ of NaNbO₃ from 300 to 673 K in the range $r \sim 1.7-4 \text{ \AA}$. Splitting of the peaks corresponding to Nb-O and Na-O interatomic correlations are marked with arrows.

trends as a function of temperature. Also, there is a sharper drop in the Q -phase fraction after 473 K. These results may indicate that the P and Q phases are structurally related, and their relative variations are related to microstructural phenomenon such as twinning [33]. In order to gain further insights into the structural relation between the $P/Q/R$ phases, we performed local structure analysis using neutron PDF data, as described below.

B. Pair-distribution function analysis of the local structure of NaNbO₃

Figure 6 shows the temperature-dependent neutron $G(r)$ of NaNbO₃ in the range of $r \sim 1.7-4.0 \text{ \AA}$, that is, for nearest- and next-nearest neighbor distances. The calculated partial PDFs for different interatomic correlations are shown in Fig. S3, and were obtained for the $Pbma$ structure. The $G(r)$ for $r \sim 1.5-2.25 \text{ \AA}$ shows the nearest-neighbor Nb-O interatomic correlations. For temperatures at or below 373 K, the Nb-O peak is clearly split with the peak centers at $r \sim 1.9 \text{ \AA}$ and $r \sim 2.1 \text{ \AA}$, which indicates an off centering of Nb within the Nb-O octahedron. Above 473 K, the two peaks for Nb-O correlations become broader and therefore they cannot be distinguished individually. However, the Nb-O peak stays asymmetric, indicating that Nb is off centered within the oxygen octahedra even at higher temperatures. The $G(r)$ in the range of $2.25 \leq r \leq 3.25 \text{ \AA}$ shows the nearest-neighbor Na-O/O-O correlations. The small shoulders that appear at $r \sim 2.5 \text{ \AA}$ and $r \sim 3.1 \text{ \AA}$ are due to a splitting of the Na-O peak into three subpeaks, which is caused by off centering of Na within the Na-O dodecahedra (see Fig. S3). Also, the O-O peak does not show any splitting. Concurrent with a broadening of the Nb-O peaks, the Na-O/O-O peaks are similarly broadened above 473 K. The broadening of the $G(r)$ peaks above 473 K indicates a thermal disordering of the structure above this temperature.

For quantitative analysis of the lattice distortions and atomic displacements within the local structure as a function of temperature, we undertook fitting of the neutron $G(r)$ using the program PDFGUI [47]. Figures 7(a) and 7(b) show results of the fitting of the neutron $G(r)$ at 300 K using either of the

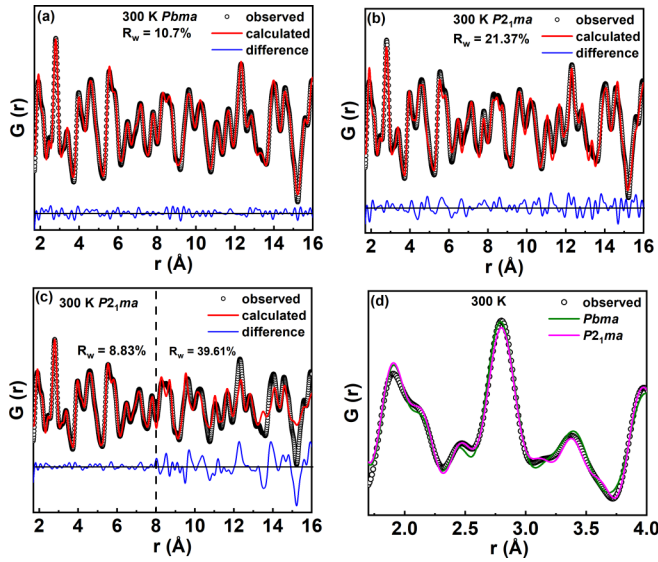


FIG. 7. Fits of neutron $G(r)$ measured at 300 K using $Pbma$ (AFE) and $P2_1ma$ (FE) structural symmetries: Comparison of fits using (a) $Pbma$ and (b) $P2_1ma$ structures over the range of $r \sim 0.17$ – 16 Å shows that the former offers a better fit. (c) Fitting of $G(r)$ over $r \sim 1$ – 8 Å using $P2_1ma$ space group provides a much-improved fit ($R_w \sim 8.83\%$), but the structure clearly deviates from local $P2_1ma$ symmetry beyond $r \sim 8$ Å, which is indicated by a higher $R_w \sim 39.61\%$ for 8 Å $< r < 16$ Å. (d) Comparison of fits using $Pbma$ and $P2_1ma$ space groups shows that the nearest- and next-nearest neighbor pairwise atomic correlations are better described by the latter.

$Pbma$ or the $P2_1ma$ structures. The starting structures in each case were obtained from the results of the Rietveld refinement using the Bragg diffraction data. If we use $Pbma$ structure (or the P phase) to fit the observed $G(r)$ over $r \sim 1.5$ – 16 Å, we obtain a reasonable fit with $R_w \sim 10.7\%$, as shown in Fig. 7(a). The fitting range over $r \sim 1.5$ – 16 Å is adopted to match with the dimension of the longer b axis of the $Pbma$ unit cell. If we use $P2_1ma$ structure (Q phase) to fit the $G(r)$ over the same distance of $r \sim 1.5$ – 16 Å, the fit is comparatively poorer ($R_w \sim 21.37\%$) as shown in Fig. 7(b), especially for $r > 8$ Å. However, if we use the space group $P2_1ma$ to fit the $G(r)$ over $r \sim 1.7$ – 8 Å, it provides a better fit for the local structure ($R_w \sim 8.83\%$), but the observed and the calculated $G(r)$ start to deviate significantly beyond 8 Å ($R_w \sim 39.61\%$) [Fig. 7(c)]. Note here that the fitting range over $r \sim 1.5$ – 8 Å matches with the dimension of the longer b axis of the $P2_1ma$ unit cell. Figure 7(d) provides a comparison between the observed $G(r)$ and the calculated $G(r)$ patterns for the $P2_1ma$ structure (refined over $r \sim 1.5$ – 8 Å) and the $Pbma$ structure (refined over $r \sim 1.5$ – 16 Å), which shows that the calculated $G(r)$ for the $P2_1ma$ structure matches better with the experimental $G(r)$ for the nearest- and next-nearest neighbor distances, that is, for $r < 4$ Å. The above analysis indicates that the local structure over nearest- and next-nearest neighbor distances can be better described by the $P2_1ma$ structure model, while the structure over longer distances, that is, at least for $r \sim 16$ Å, starts to deviate from the $P2_1ma$ structure. Differences between the local and longer-range structures for NaNbO_3 , such as ob-

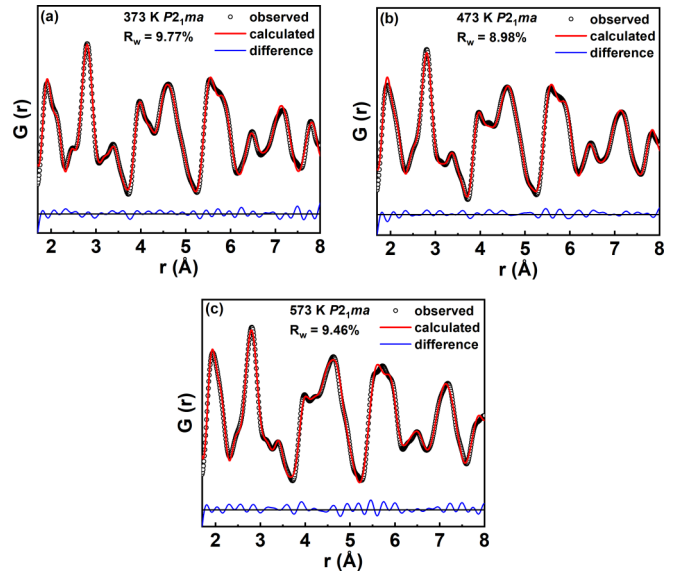


FIG. 8. Fits of neutron $G(r)$ for interatomic distance $r \sim 1.7$ – 8 Å, using $P2_1ma$ space-group structures at temperatures: (a) 373 K, (b) 473 K, and (c) 573 K.

served here, are consistent with the earlier report by Jiang *et al.* [34]. However, Jiang *et al.* used an $R3c$ structure to fit the short-range $G(r)$ [34]. We tried to fit the short-range $G(r)$ with an $R3c$ structure model; however, it provided a worse fit ($R_w \sim 24.15\%$) as compared to the $P2_1ma$ structure ($R_w \sim 8.83\%$) (Supplemental Material, Fig. S4 [46]). Similar to what is observed at 300 K, the $G(r)$ measured at temperatures 373, 473, and 573 K could all be better reproduced using the $P2_1ma$ structure for $r < 8$ Å, as shown in Figs. 8(a)–8(c). Also, comparison of PDF fits for the $P2_1ma$ and $Pbma$ structures at all temperatures shows that the former can better reproduce the experimental PDF for nearest- and next-nearest neighbor distances, i.e., below 4 Å (Figs. S5, S6, and S7 in the Supplemental Material [46]). This shows that even though the Bragg diffraction data indicate that the volume fraction of the antiferroelectric P phase increases with increasing temperature, the structure over $r \sim 8$ Å appears to resemble that of the ferroelectric Q phase. However, as noted above, the structure deviates from an ideal $P2_1ma$ symmetry beyond 8 Å for all the measurement temperatures from 300 K $\leq T \leq 573$ K (Fig. S8 in the Supplemental Material [46]).

For the $G(r)$ measured at 673 K, we tried both the $Pmnm$ and $Pnma$ space groups, since either of these structures could be used to fit the Bragg diffraction data equally well. As can be observed from Fig. 9, both the $Pmnm$ and $Pnma$ structures provide equally good fits to the observed $G(r)$ with $R_w \sim 9.88\%$ and $R_w \sim 9.95\%$, respectively. Note that we used a box-size of $r \sim 1.7$ – 24 Å to match with the longer dimension of the $Pmnm/Pnma$ unit cells. We also tried with $Pbma$ and $P2_1ma$ structure models to fit the measured $G(r)$ at 673 K, as shown in Figs. S9(a) and S9(b) in Supplemental Material [46]; however, they provided worse fits ($R_w \sim 12.91\%$ for $Pbma$ and $R_w \sim 10.77\%$ for $P2_1ma$) as compared to the $Pmnm$ or $Pnma$ structures. Therefore, the local structure above the phase-transition temperature of ~ 615 K clearly deviates from that at lower temperatures. However, based on the $G(r)$ data

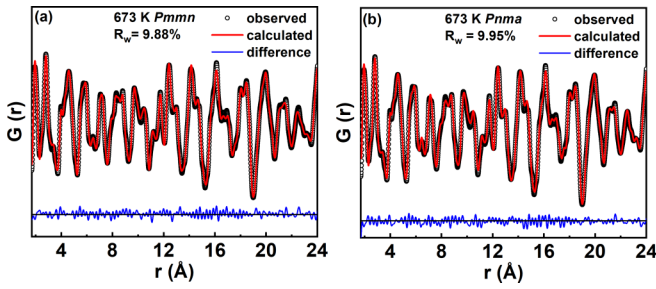


FIG. 9. Fits of neutron $G(r)$ measured at 673 K over (a) $r \sim 1.7\text{--}24 \text{ \AA}$, using $Pmnm$ space group and (b) $r \sim 1.7\text{--}24 \text{ \AA}$, using $Pnma$ space group.

alone it is not possible to distinguish between the appropriateness of either the $Pmnm$ or $Pnma$ models for describing the local structure.

C. Comparison of the local and average structures

In earlier studies of NaNbO_3 , it was noted that both the P and Q phases coexist for $T < 633 \text{ K}$, although their relative volume fractions could be different depending on processing methods and probing techniques [18,33,35,41,42]. From a structural point of view, the P and Q phases are similar, while the transition between them is associated with subtle changes in the oxygen octahedral tilt arrangements and Na/Nb off-centering displacements. Below, we explore the structural relationship between the P and Q phases based on the current refinement results of the average and local structures.

The average structure of the P phase, which is obtained from Rietveld refinement of the neutron Bragg diffraction data, exhibits a $Pbma$ symmetry as illustrated in Fig. 10(a).

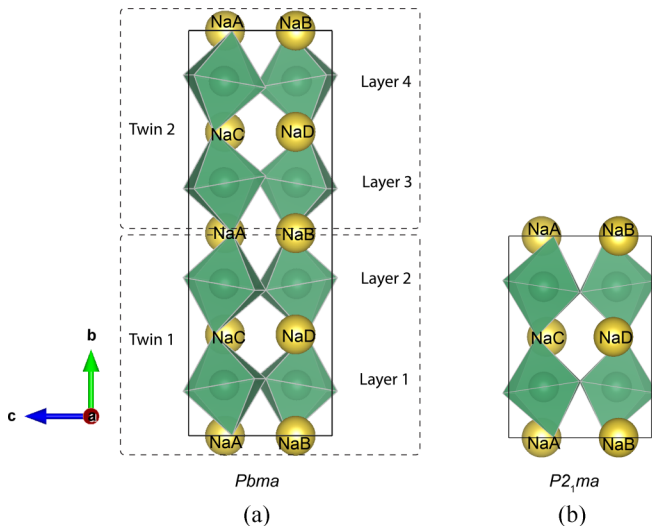


FIG. 10. Representation of (a) the P - ($Pbma$) and (b) the Q - ($P2_1ma$) phase structures. The octahedral tilting within the layers 1 and 2 of the $Pbma$ unit cell are identical to that of the $P2_1ma$ unit cell shown on the right. The octahedral tilting within the layers 3 and 4 of the $Pbma$ unit cell are obtained by rotating the $P2_1ma$ shown on the right by 180° around the b axis. The labels for Na correspond to those within the local $P2_1ma$ local structure.

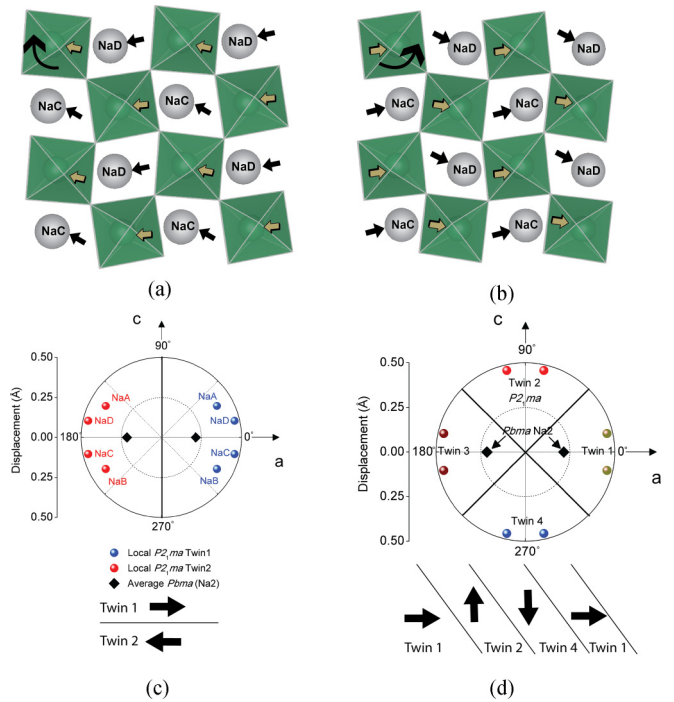


FIG. 11. (a), (b) The atomic arrangements within the octahedral layers of 180° twins of the $P2_1ma$ local structure (refer to Fig. 10.). Note that only NaC/NaD are shown, which are located fully within each $P2_1ma$ structural block. (c) Polar plot showing direction of Na atom displacements within individual 180° twin variants. (d) Polar plot showing direction of Na atom (only NaC/NaD) displacements within a possible arrangement non- $180^\circ/180^\circ$ twin variants, such as depicted below.

The unit-cell parameters of the P phase are given by $\sqrt{2}a_p \times 4b_p \times \sqrt{2}c_p$, where the subscript p refers to the pseudocubic unit of ABO_3 perovskite. In Fig. 10(a), the four octahedral layers along the b axis are marked as 1–4. The octahedral tilts around the b axis in the layers 1(3) and 2(4) are in phase, whereas there is an out-of-phase tilt between the layers 2 and 3. The octahedral tilting arrangement in the P phase, following Glazer notation, can be stated as $a^-b^+c^-/a^-b^-c^-/a^-b^+c^-$ [33]. Figure 10(b) shows the average structure of the Q phase with the $P2_1ma$ symmetry. As compared to the P phase, it exhibits a simpler octahedral tilt pattern of $a^-b^+c^-$, and the unit-cell parameters are given by $\sqrt{2}a_p \times 2b_p \times \sqrt{2}c_p$. That is, the dimension of the unit cell of the Q phase along the longer b axis is approximately half of that of the P phase. Based on this, Johnston *et al.* proposed that the P phase results as a consequence of a “twinning” operation, whereby the layers 3/4 of the P phase in Fig. 10(a) results from a 180° reorientation of the layers 1/2. The two-layer blocks comprising layers 1 and 2 or 3 and 4 in Fig. 10(a) correspond to one unit cell of the Q phase, which are rotated with respect to each other by 180° [33]. In other words, the $Pbma$ symmetry reflects the average structure of several twin variants, while the local structure is of the $P2_1ma$ symmetry. We examine below this hypothesis in detail based on the current refinement results of the local and average structures.

Figure 11(a) shows the atomic arrangement within a single octahedral layer of the local $P2_1ma$ structure, which is

obtained from fitting of the neutron $G(r)$ data over $r \sim 1.7\text{--}8 \text{ \AA}$. Note that this corresponds to the layers 1 and 2 of the average P -phase structure with $Pbma$ symmetry shown in Fig. 10(a). The arrows in Fig. 11(a) indicate the directions of in-plane off-centering displacements of Na and Nb atoms within their respective surrounding oxygen cages. Figure 11(b) shows the resultant local structure from a 180° twinning operation of the local $P2_1ma$ structure shown in Fig. 11(a). In Figs. 11(a) and 11(b), the Na are labeled individually in the local structure, so as to distinguish between them. The same labels that are used in Figs. 11(a) and 11(b) are also used to mark the equivalent Na atom sites in the P or Q -phase structures shown in Figs. 10(a) and 10(b). Here, NaA and NaB (NaC and NaD) are used to mark the Na atom sites in the local $P2_1ma$ structure, which correspond to the Na1(Na2) sites of the average P -phase structure. The directional off-centering displacements of Na atoms within the a - c plane, for the two 180° twins with local $P2_1ma$ structure, are shown using a polar plot in Fig. 11(c). The corresponding Na2 displacements along a axis within the average P ($Pbma$) phase structure are superimposed as black diamonds on those of the twinned $P2_1ma$ structures. Please note that for the average P -phase structure, Na1 exhibits zero off centering, while the Na2 atoms in the top and bottom halves of the unit cell exhibit out-of-phase or antipolar displacements. If we consider that the average P -phase structure consists of two 180° twin variants of the local $P2_1ma$ structures, then the NaA/NaB atoms are shared between the neighboring 180° twins, while the NaC/NaD are placed fully within the individual twin variants. Figure 11(c) elegantly illustrates the spatial averaging of the Na positions caused by stacking of the octahedral layers in this twin arrangement. An averaging of the instantaneous off-centering displacements of the NaA/NaB atoms of the local $P2_1ma$ structures of the neighboring twin variants results in a zero displacement of Na1 in the $Pbma$ unit cell of the average P -phase structure. Since NaA/NaB are shared by both the twin variants, their positions shown in Fig. 11(c) can be understood as the maximum instantaneous Na displacements at these positions. The averaging of the instantaneous displacements of NaC/NaD of the local $P2_1ma$ structure results in net antipolar displacements for Na2 along the a axis in the $Pbma$ unit cell of the average P -phase structure. Since NaC/NaD of the local $P2_1ma$ structures are placed fully within the respective twin blocks, their out-of-phase displacements are preserved in the $Pbma$ structure unit cell of the average P -phase structure. Also note from Fig. 11(c) that, in contrast to NaC/NaD, NaA/NaB show displacement directions that are deviated further away from the a -axis direction, since their neighboring octahedra are tilted out of phase with each other. It is noteworthy, however, that the magnitude of off-centered displacement of Na2 in the average P -phase ($Pbma$) structure is less than that of the average displacement of NaC/NaD in the local $P2_1ma$ structures. This could arise due to complex twin arrangements such as illustrated in Fig. 11(d). Figure 11(d) depicts the displacements of NaC/NaD for an alternative scenario of twins, for which an averaging of the NaC/NaD displacements, such as for stacking of twin1/twin2/twin4/twin1 shown in Fig. 11(d), results in a net Na displacement that is closer to the displacement of Na2 in the average P - ($Pbma$) phase structure. In reality, both 180° and non- 180° twin variants of local

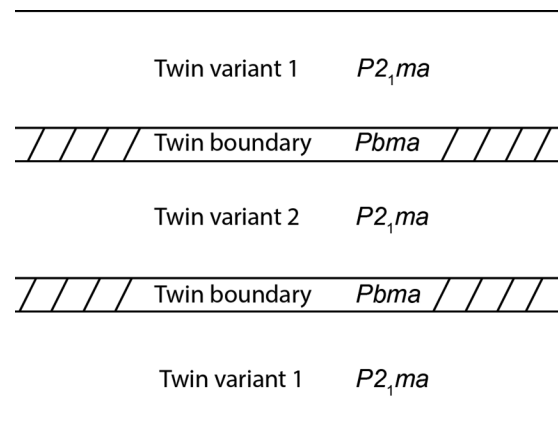


FIG. 12. Schematic representation of a possible 180° twin structure. For regions within each twin variant, the octahedra are rotated in phase around the b axis, and therefore exhibits the $P2_1ma$ symmetry or Q phase. Across each twin boundary, the octahedra are rotated out of phase around the b axis, and therefore exhibit $Pbma$ symmetry or P phase. The relative fractions of the P and Q phases will change with change in volume of twin boundary regions with respect to the twin variants.

$P2_1ma$ structural units are possible in a NaNbO_3 material sample. Complex domain arrangements in antiferroelectric ceramics have been reported earlier in studies such as Refs. [48,49].

Based on the above description, the relative volume fraction of the P and Q phases would depend on the width of the twin variants, such as illustrated in Fig. 12. The volume within the bulk of a twin variant would correspond to the Q phase, while the region adjacent to a 180° twin boundary would correspond to the P phase. Therefore, the relative volume fraction of the P phase will be greater for smaller width of the twin variants. In Fig. 5(d), it is shown that the relative volume fraction of the Q phase decreases with increasing temperature. We attribute this to a reformation of the twin microstructure in the form of decrease in the width of the twin variants with increasing temperature. A microstructural change, rather than a strict atomic structural change, for Q -to- P transformation is also consistent with the DSC data shown in Fig. 1(a), which shows a broad hump in the range of $300 \text{ K} \leq T \leq 600 \text{ K}$ instead of a sharp peak.

A rationale for a finer twin structure at higher temperatures can be deduced from the temperature-dependent local atomic structure. Figures 13(a) and 13(b) show the average Na and Nb off centering within their surrounding oxygen cages for the local structure as a function of temperature. At 300 K, Na is off centered within the O dodecahedra by $\sim 0.42 \text{ \AA}$, which is similar to the result obtained by Jiang *et al.* [34]. Similarly, the average Nb off centering within the O octahedra is $\sim 0.25 \text{ \AA}$. Such rather large off centerings of Na and Nb at 300 K are expected to cause high-energy barriers for their motion between symmetry-equivalent positions, which would result in a trapping of the Na and Nb atoms at their respective local positions. In other words, the twin structure is “frozen” in the as-synthesized state at low temperatures. With increasing temperatures, the off-centering displacements of both Na and Nb decrease, with consequent decrease in energy barriers for their

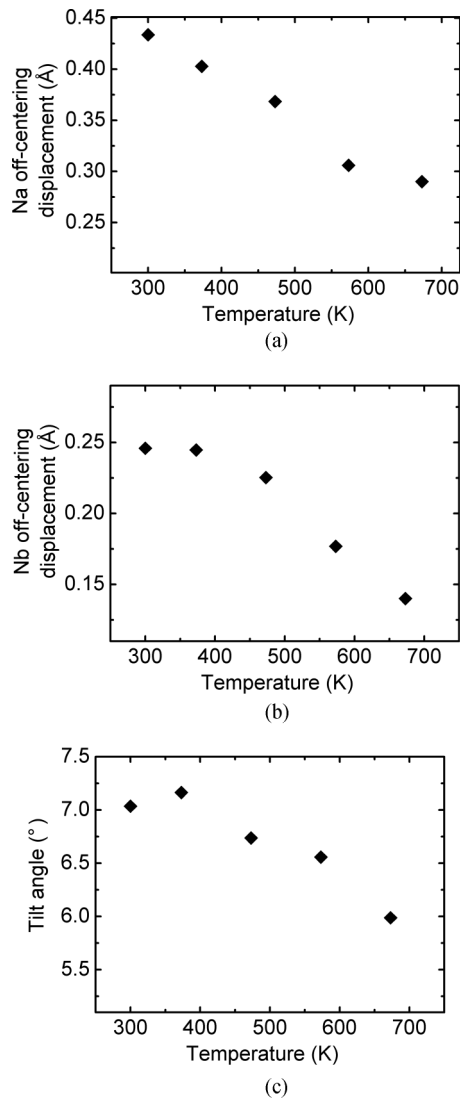


FIG. 13. (a), (b) Cation off-centering displacements within the surrounding oxygen polyhedral: (a) Na displacement within the surrounding oxygen dodecahedra, (b) Nb displacement within the surrounding oxygen octahedra, and (c) the NbO_6 octahedral tilting angle.

motion between symmetry-equivalent positions. Also note from Fig. 13(c) that the tilting angle around the b axis decrease with increasing temperature. Both of these factors, together with higher thermal activation at higher temperatures, can lead to a reconstruction of the as-synthesized twin microstructure resulting in smaller twin variants, and consequently a higher volume fraction of the P phase.

Figures 14(a) and 14(b) depict views of the average $Pnma$ and $Pm\bar{m}n$ structures of the R phase at 673 K. Neither of these structures can be explained as a simple twinning operation of the local $P2_1ma$ structure at lower temperatures. Rather, it appears that the R phase results from a true crystal structural phase transition. This is also consistent with a sharp peak in the DSC data at $T \sim 615$ K, shown in Fig. 1(a). Although both $Pnma$ and $Pm\bar{m}n$ provide equally good fit for the measured neutron $G(r)$, the two structures show slightly different local chemical environments for the Na atom sites.

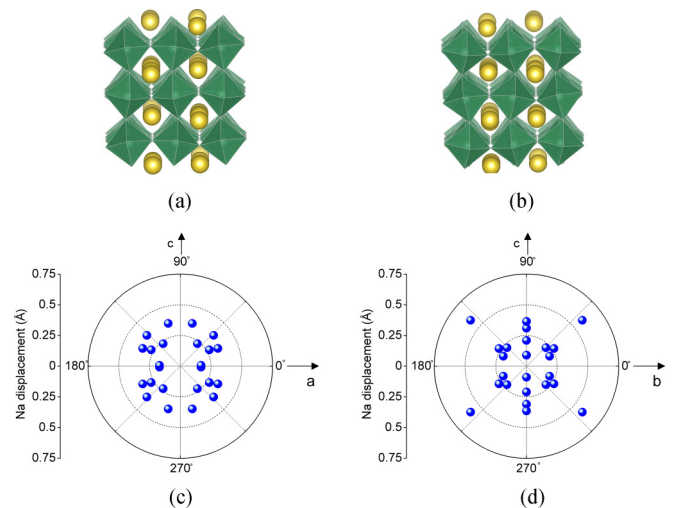


FIG. 14. Representations of the average structure of the R phase, following the (a) $Pnma$, and (b) $Pm\bar{m}n$ symmetries. Polar plot showing Na off-centering displacement directions within the oxygen dodecahedra of the different layers of the (c) $Pnma$ and (d) $Pm\bar{m}n$ structures.

Figure 14(c) shows the Na off-centering displacements within the local $Pnma$ structure, which are much more disordered as compared to those within the local $P2_1ma$ structure at lower temperatures [e.g., see Figs. 11(c) and 11(d)]; this is also reflected by the significantly broadened PDF peak for Na-O in Fig. 6. The increased disordering of Na within the oxygen cage can be related to a disordering of the NbO_3 octahedral tilting, which changes the immediate neighborhood for the Na atoms. In the local $Pnma$ structure, the directions of Na displacements within the surrounding O cage are uniformly distributed around a circle of radius ~ 0.30 Å in the $a-c$ plane, as shown in Fig. 14(c). In contrast, Na off-centering displacements within the local $Pm\bar{m}n$ structure appear as a bimodal distribution centered around ~ 0.25 and ~ 0.60 Å, as shown in Fig. 14(d). Given that the local chemical environment is likely to be similar for all the Na atomic sites, the local structure is more likely to be $Pnma$, even though both $Pnma$ and $Pm\bar{m}n$ could provide equally good fits to the x-ray/neutron-diffraction and $G(r)$ patterns (Ref. [41] and present study). Therefore, based on an analysis of the neutron PDF data, the transition to R phase at 615 K results from a disordering of the local Na off-centering displacements within their surrounding O cages, which can be approximated as a $P2_1ma$ to $Pnma$ structural transformation.

IV. CONCLUSION

In summary, we have used neutron powder diffraction and neutron pair-distribution function analyses to characterize the relationship between the average and local structural phases of NaNbO_3 , especially with reference to transformations between the AFE and FE phases as a function of temperature. Intriguingly, earlier studies on NaNbO_3 provided conflicting results about the coexistence of AFE P ($Pbma$) and FE Q ($P2_1ma$) phases. Here, based on an analysis of x-ray and neutron diffraction, and neutron $G(r)$ data, we showed that the

P and Q phases can indeed be related to each other through $180^\circ/90^\circ$ twinning operation of elementary local structural blocks with $P2_1ma$ symmetry. Furthermore, changes in the relative fractions of the P and Q phases can be derived from a refinement of the twin structure. However, transformation from the P phase to the R phase at higher temperatures cannot be described as a twinning operation, but rather occurs as a result of further disordering of Na displacement directions within the oxygen dodecahedra. These insights resolve earlier conflicting reports on coexistence and transformation between AFE and FE phases of NaNbO_3 and may help in better design of solid solutions of NaNbO_3 with stabilized AFE/FE phases.

ACKNOWLEDGMENTS

The work described in this paper was partially supported by a grant from the Research Grants Council of the Hong Kong Special Administrative Region, China (Project No.

CityU 11306720). Funding support from City University of Hong Kong (Project No. CityU 7005644) is gratefully acknowledged. F.M., D.R.S., and M.R.V.J. thank the Danish Agency for Science, Technology, and Innovation for funding the instrument center DanScatt. Affiliation with the Center for Integrated Materials Research (iMAT) at Aarhus University is gratefully acknowledged. We acknowledge MAX IV Laboratory for time on DanMAX. Research conducted at MAX IV, a Swedish national user facility, is supported by the Swedish Research council under Contract 2018–07152, the Swedish Governmental Agency for Innovation Systems under Contract No. 2018–04969, and Formas under Contract No. 2019–02496. DanMAX is funded by the NUFU Grant No. 4059-00009B. A portion of this research used resources at the Spallation Neutron Source, a DOE Office of Science User Facility operated by the Oak Ridge National Laboratory (Grant No. IPTS-27376 for POWGEN and NOMAD experiments).

-
- [1] M. E. Lines and A. M. Glass, *Principles and Applications of Ferroelectrics and Related Materials* (Oxford University Press, Oxford, UK, 1977).
- [2] *Physics of Ferroelectrics*, edited by K. M. Rabe, C. H. Ahn, and J. Triscone (Springer, Heidelberg, Germany, 2007).
- [3] I. Lefkowitzk, K. Lukazewicz, and H. D. Megaw, *Acta Crystallogr.* **20**, 670 (1966).
- [4] A. C. Sakowski-Cowely, K. Lukazewicz, and H. D. Megaw, *Acta Crystallogr., Sect. B: Struct. Crystallogr. Cryst. Chem.* **25**, 851 (1969).
- [5] M. Ahtee, A. M. Glazer, and H. D. Megaw, *Philos. Mag.* **26**, 995 (1972).
- [6] A. M. Glazer and H. D. Megaw, *Philos. Mag.* **25**, 1119 (1972).
- [7] N. W. Darlington and H. D. Megaw, *Acta Crystallogr., Sect. B: Struct. Crystallogr. Cryst. Chem.* **B29**, 2171 (1973).
- [8] A. M. Glazer and H. D. Megaw, *Acta Crystallogr., Sect. A: Cryst. Phys., Diffraction, Theor. Gen. Crystallogr.* **A29**, 489 (1973).
- [9] H. D. Megaw, *Ferroelectrics* **7**, 87 (1974).
- [10] C. N. W. Darlington and K. S. Knight, *Physica B* **266**, 368 (1999).
- [11] C. N. W. Darlington and K. S. Knight, *Acta Crystallogr., Sect. B: Struct. Sci.* **55**, 24 (1999).
- [12] Yu. I. Yuzyuk, P. Simon, E. Gagarina, L. Hennem, D. Thiaudiere, V. I. Torgashev, S. I. Raevskaya, I. P. Raevskii, L. A. Reznitchenko, and J. L. Sauvajol, *J. Phys.: Condens. Matter* **17**, 4977 (2005).
- [13] Yu. I. Yuzyuk, E. Gagarina, P. Simon, L. A. Reznitchenko, L. Hennem, and D. Thiaudiere, *Phys. Rev. B* **69**, 144105 (2004).
- [14] E. Bouizane, M. D. Fontana, and M. Ayadi, *J. Phys.: Condens. Matter* **15**, 1387 (2003).
- [15] R. J. C. Lima, P. T. C. Freire, J. M. Saski, A. P. Ayala, F. E. A. Melo, J. Mendes Filho, K. C. Serra, S. Lanfredi, M. H. Lente, and J. A. Eiras, *J. Raman Spectrosc.* **33**, 669 (2002).
- [16] Z. X. Shen, X. B. Wang, M. H. Kuok, and S. H. Tang, *J. Raman Spectrosc.* **29**, 379 (1998).
- [17] X. B. Wang, Z. X. Shen, Z. P. Hu, L. Qin, S. H. Tang, and M. H. Kuok, *J. Mol. Struct.* **385**, 1 (1996).
- [18] S. K. Mishra, N. Choudhury, S. L. Chaplot, P. S. R. Krishna, and R. Mittal, *Phys. Rev. B* **76**, 024110 (2007).
- [19] Y. Shiratori, A. Magrez, J. Dornseiffer, F.-H. Haegel, C. Pithan, and R. Waser, *J. Phys. Chem. B* **109**, 20122 (2005).
- [20] Y. Shiratori, A. Magrez, M. Kato, K. Kasezawa, C. Pithan, and R. Waser, *J. Phys. Chem. C* **112**, 9610 (2008).
- [21] H. Guo, H. Shimizu, and C. A. Randall, *App. Phys. Lett.* **107**, 112904 (2015).
- [22] C. A. Randall, Z. Fan, I. Reaney, L.-Q. Chen, and S. Trolier-McKinstry, *J. Am. Ceram. Soc.* **104**, 3775 (2021).
- [23] J. Chen, H. Qi, R. Zuo, and A. C. S. App, *Mater. Interfaces* **12**, 32871 (2020).
- [24] H. Qi, R. Zuo, A. Xie, A. Tian, J. Fu, Y. Zhang, and S. Zhang, *Adv. Funct. Mater.* **29**, 1903877 (2019).
- [25] B. Luo, H. Dong, D. Wang, and K. Jin, *J. Am. Ceram. Soc.* **101**, 3460 (2018).
- [26] E. L. Falcao-Filho, C. A. C. Bosco, G. S. Maciel, L. H. Acioli, C. B. de Araujo, A. A. Lipovskii, and D. K. Tagantsev, *Phys. Rev. B* **69**, 134204 (2004).
- [27] J. H. Jung, M. Lee, J.-I. Hong, Y. Dong, C.-Y. Chen, L.-J. Chou, and Z. L. Wang, *ACS Nano* **5**, 10041 (2011).
- [28] F. Li, K. Li, M. Long, C. Wang, G. Chen, and J. Zhai, *Appl. Phys. Lett.* **118**, 043902 (2011).
- [29] M. Kosec, B. Malic, A. Bencan, and T. Rojac, in *Piezoelectric and Acoustic Materials for Transducer Applications* (Springer, Boston, MA, 2008), pp. 81–102.
- [30] L. Gao, H. Guo, S. Zhang, and C. A. Randall, *J. Appl. Phys.* **120**, 204102 (2016).
- [31] A. Xie, H. Qi, R. Zuo, A. Tian, J. Chen, and S. Zhang, *J. Mater. Chem. C* **7**, 15153 (2019).
- [32] H. Shimizu, H. Guo, S. E. Reyes-Lillo, Y. Mizuno, K. M. Rabe, and C. A. Randall, *Dalton Trans.* **44**, 10763 (2015).
- [33] K. E. Johnston, C. C. Tang, J. E. Parker, K. S. Knight, P. Lightfoot, and S. E. Ashbrook, *J. Am. Chem. Soc.* **132**, 8732 (2010).
- [34] L. Jiang, D. C. Mitchell, W. Dmowski, and T. Egami, *Phys. Rev. B* **88**, 014105 (2013).

- [35] K. E. Johnston, J. M. Griffin, R. I. Walton, D. M. Dawson, P. Lightfoot, and S. E. Ashbrook, *Phys. Chem. Chem. Phys.* **13**, 7565 (2011).
- [36] G. Ashiotis, A. Deschildre, Z. Nawaz, J. P. Wright, D. Karkoulis, F. E. Picca, and J. Kieffer, *J. Appl. Cryst.* **48**, 510 (2015).
- [37] A. Huq, M. J. Kirkham, P. F. Peterson, J. P. Hodges, P. Whitfield, K. Page, T. Huegle, E. B. Iverson, A. Parizzi, and G. Q. Rennich, *J. Appl. Crystallogr.* **52**, 1189 (2019).
- [38] J. Neufeind, M. Feygenson, J. Carruth, R. Hoffmann, and K. K. Chipley, *Nucl. Instrum. Methods Phys. Res. Sect. B* **287**, 68 (2012).
- [39] T. Egami and S. J. L. Billinge, *Underneath the Bragg Peaks: Structural Analysis of Complex Materials* (Elsevier, Oxford, England, 2003).
- [40] D. A. Keen, *J. Appl. Crystallogr.* **34**, 172 (2001).
- [41] M. D. Peel, S. P. Thompson, A. Daoud-Aladine, S. E. Ashbrook, and P. Lightfoot, *Inorg. Chem.* **51**, 6876 (2012).
- [42] S. K. Mishra, R. Mittal, V. Y. Pomjakushin, and S. L. Chaplot, *Phys. Rev. B* **83**, 134105 (2011).
- [43] B. H. Toby and R. B. Von Dreele, *J. Appl. Crystallogr.* **46**, 544 (2013).
- [44] H. Xu, Y. Su, M. Lou Balmer, and A. Navrotsky, *Chem. Mater.* **15**, 1872 (2003).
- [45] L. B. McCusker, R. B. Von Dreele, D. E. Cox, D. Louër, and P. Scardi, *J. Appl. Crystallogr.* **32**, 36 (1999).
- [46] See Supplemental Material at <http://link.aps.org/supplemental/10.1103/PhysRevB.105.174113> for additional information on Rietveld refinement and fitting of neutron G(r) data.
- [47] C. L. Farrow, P. Juhas, J. W. Liu, D. Bryndin, E. S. Bozin, J. Bloch, T. Proffen, and S. J. L. Billinge, *J. Phys.: Condens. Matter* **19**, 335219 (2007).
- [48] T. Ma, Z. Fan, X. Tab, and L. Zhou, *Appl. Phys. Lett.* **115**, 122902 (2019).
- [49] I. MacLaren, L. Wang, O. Morris, A. J. Craven, R. L. Stamps, B. Schaffer, Q. M. Ramasse, S. Miao, K. Kalantari, I. Sterianou, and I. M. Reaney, *APL Mater.* **1**, 021102 (2013).